



UNIVERSITÀ DI PARMA

ARCHIVIO DELLA RICERCA

University of Parma Research Repository

Experimental and numerical analysis of side weir flows in a converging channel

This is the peer reviewed version of the following article:

Original

Experimental and numerical analysis of side weir flows in a converging channel / Maranzoni, Andrea; Pilotti, Marco; Tomirotti, Massimo. - In: JOURNAL OF HYDRAULIC ENGINEERING. - ISSN 0733-9429. - 143:7(2017), pp. 04017009-1-04017009-15. [10.1061/(ASCE)HY.1943-7900.0001296]

Availability:

This version is available at: 11381/2823485 since: 2021-10-14T16:11:40Z

Publisher:

American Society of Civil Engineers (ASCE)

Published

DOI:10.1061/(ASCE)HY.1943-7900.0001296

Terms of use:

Anyone can freely access the full text of works made available as "Open Access". Works made available

Publisher copyright

note finali coverpage

(Article begins on next page)

EXPERIMENTAL AND NUMERICAL ANALYSIS OF SIDE WEIR FLOWS IN A CONVERGING CHANNEL

Andrea Maranzoni¹; Marco Pilotti²; and Massimo Tomirotti³

¹ PhD, Researcher, DICATeA, University of Parma, Parco Area delle Scienze 181/A, 43124 Parma, Italy. E-mail: andrea.maranzoni@unipr.it

² PhD, Associate Professor, DICATAM, University of Brescia, Via Branze 43, 25123 Brescia, Italy. E-mail: marco.pilotti@unibs.it

³ PhD, Associate Professor, DICATAM, University of Brescia, Via Branze 43, 25123 Brescia, Italy. E-mail: massimo.tomirotti@unibs.it

Abstract This paper investigates the lateral outflow over a short-crested side weir inserted in a converging rectangular channel with linearly decreasing width in the flow direction. This type of overflow device induces a spatially varied free-surface flow with decreasing discharge and, due to the convergent geometry, it can potentially improve the performance of the distribution channels commonly used in irrigation systems, sewer networks, waste-water plants, and hydropower facilities for flow diversion and control, and for flood protection. A laboratory investigation is carried out to analyze the main hydraulic characteristics of this kind of flow and assess the improvement in outflow efficiency compared to the conventional rectangular side weir in a prismatic channel. Only subcritical steady flow conditions are considered. Experimental data show that the Froude number in the main channel downstream of the weir and the dimensionless weir height are significant variables to describe the outflow efficiency, and confirm that the non-prismaticity of the main channel induces a noticeable increase in outflow performance. Furthermore, the experimental results show that the assumption of constant specific energy usually adopted in one-dimensional side weir flow modeling is reasonably valid, despite the considerable increase in the velocity-head and momentum correction coefficients along the side weir. Finally, the comparison between experimental data and numerical results shows that the classic one-dimensional modeling approach can adequately predict the main engineering aspects of side weir flows in non-prismatic channels.

Subject headings: side weir, lateral outflow, non-prismatic channel, outflow efficiency, experiments, spatially varied flow

32 **Introduction**

33 Side weirs are ubiquitous hydraulic devices used in irrigation systems, sewer networks, waste-water plants,
34 hydropower facilities, and flood mitigation works to divert flow laterally for distribution and control purposes, thereby
35 giving rise to a spatially varied flow with decreasing discharge in the flow direction. Accordingly, side weirs have been
36 extensively studied in literature from both theoretical and experimental perspectives. In particular, special attention has
37 been devoted in the past to the conventional rectangular sharp-crested side weir, parallel to the flow direction and
38 inserted in a prismatic rectangular channel.

39 The one-dimensional (1D) approach is widely used to model spatially varied flows with decreasing discharge (e.g.
40 Chow, 1959; Castro-Orgaz and Hager, 2012), and in general in river hydraulics (e.g. Cunge et al., 1980; Pilotti et al.,
41 2011). A theoretical 1D analysis based on the assumption of constant specific energy along the side weir was first
42 proposed by De Marchi (1934), who derived an analytical solution for the equation of the flow profile in the channel.
43 The 1D schematization has also been applied to spatially varied steady flows in non-prismatic rectangular open
44 channels with both decreasing (Yen and Wenzel, 1970; Hager and Volkart, 1986; Hager, 1999) or increasing discharge
45 (Kouchakzadeh and Vatankhah Mohammad-Abadi, 2002; Citrini, 1942). However, the adoption of the classic weir
46 formula to characterize the overflowing discharge per unit length introduces a discharge coefficient in the mathematical
47 model which must be empirically assessed. With this aim, the hydraulic characteristics of the outflow over sharp-
48 crested side weirs have been widely investigated in literature from an experimental point of view in the last decades,
49 typically in subcritical steady flow conditions (e.g., Hager, 1987; Novak et al., 2013) but also in supercritical flows
50 (e.g., Hager, 1987; Uyumaz, 1997). The basic model hypothesis of constant specific energy along the side weir has been
51 verified on the basis of the experimental data collected in extensive laboratory studies (e.g. El-Khashab and Smith,
52 1976; Borghei et al. 1999), and suitable mathematical models of the functional dependence of the steady-state discharge
53 coefficient on some dimensionless flow and geometrical variables have been calibrated (e.g., Subramanya and Awasthy,
54 1972; Nandesamoorthy and Thomson, 1972; Ranga Raju et al., 1979; Ramamurthy and Carballada, 1980; Singh et al.,
55 1994; Jalili and Borghei, 1996; Borghei et al., 1999, Emiroglu et al., 2011). The three-dimensional (3D) flow structures
56 induced by the lateral diversion have also been investigated along with the direct implications on 1D modelling
57 (Michelazzo et al., 2015), and the spatial variation of the discharge coefficient along the side weir has been analyzed too
58 (e.g. Swamee et al., 1994; Aghayari et al., 2009). Most research has focused on sharp-edged weirs, but recently broad-
59 crested side weirs have also been considered in literature (e.g. Aghayari et al., 2009; Haddadi and Rahimpour, 2012;
60 Řiha and Zachoval, 2014).

61 The arrangement of side weirs in a straight prismatic channel is common and easy to implement but may suffer from
62 low overall efficiency. A feasible way to overcome this problem is to increase the effective weir crest length. Therefore,
63 oblique (e.g. Ura et al., 2001; Borghei and Parvaneh, 2011; Parvaneh et al., 2012) and labyrinth side weirs (e.g.

64 Emiroglu et al., 2010; Parvaneh et al., 2011) installed in prismatic channels have been recently investigated in literature
65 to assess the improvement in outflow efficiency in various situations.

66 Another effective and common modality to enhance the efficiency of conventional side weirs is based on the
67 introduction of either a low hump on the channel bottom, or a channel constriction (induced by a lateral cross-section
68 contraction and/or by an underflow gate) downstream of the weir, with the aim of creating a backwater effect and
69 increasing the head over the weir crest. However, these solutions are not devoid of contraindications: a hump may cause
70 sedimentation, and a sluice gate may interact negatively with floating debris. Moreover, if the flow diversion reduces
71 the channel discharge significantly, a constant channel width can be economically unjustified and may even turn into a
72 problem when low average velocities trigger sedimentation in the onward flow channel.

73 Accordingly, an alternative means to improve the outflow performance is to insert the side weir in a non-prismatic
74 converging channel exploiting the reduction of the channel width, as well as the oblique alignment of the side weir with
75 reference to the main flow direction. In this way, the effective length of the weir increases slightly for a given main
76 channel stretch and the incoming flow velocity acquires a component orthogonal to the weir. In any case, the decrease
77 in the channel conveyance along the flow diverting device is consistent with the progressively decreasing discharge in
78 the main channel. Despite the above mentioned advantages, to the authors' knowledge relatively little attention has been
79 devoted to the study of oblique weirs in converging channels. For instance, Gissoni and Hager (1997) analyzed short
80 sewer side weirs inserted in U-shaped converging channels. Honar and Javan (2007) provided an empirical relation
81 between the discharge coefficient and the angle of inclination of the side weir with reference to the main flow direction
82 and, more recently, Říha and Zachoval (2014) experimentally investigated the discharge coefficient of trapezoidal
83 broad-crested side weirs with different oblique angles.

84 This paper provides a contribution in this direction by presenting a laboratory and numerical analysis of the
85 performance of a one-side short-crested weir placed along the oblique side of a converging rectangular channel, in fixed
86 bed and subcritical steady flow conditions. The main objectives of this work are to: (1) describe the physical features of
87 a side weir flow in a converging main channel; (2) analyze the variation of the velocity-head and momentum correction
88 coefficients along the side weir; (3) check the validity of the assumption of constant specific energy in the case of a
89 non-prismatic channel; (4) verify the improvement in outflow efficiency, compared with the conventional rectangular
90 side weir in a prismatic channel; (5) provide a reliable assessment of the steady-flow discharge coefficient, which is an
91 essential requirement for applications; and finally, (6) assess the capability of the 1D approach to accurately predict the
92 main engineering aspects of the flow by comparing experimental data and numerical results.

93 The first section of the paper briefly recalls the basic concepts of the 1D theory of spatially varied steady flows with
94 decreasing discharge in gradually converging channels. The second section reports a dimensional analysis of this type
95 of flows. The third section describes the experimental set-up and details the test conditions of the laboratory

96 investigation. The results of the experimental and numerical analysis are presented and discussed in the fourth section.
 97 Finally, some conclusions are drawn in the last section.

98

99 **Theoretical Background**

100 Spatially varied steady flows with non-uniform discharge are commonly described using the 1D approach, which
 101 assumes that the pressure is hydrostatic and the bottom slope of the main channel is small (e.g., Chow, 1959; Hager and
 102 Volkart, 1986).

103 The following dynamic equation can be derived by applying the momentum principle to a spatially varied steady
 104 flow with decreasing discharge in a non-prismatic open-channel (Yen and Wenzel, 1970):

$$105 \quad \frac{dh}{dx} = \frac{S_0 - S_f - \frac{Q}{gA^2} \left(2\beta - \frac{A}{Q} V \cos \varphi \right) \frac{dQ}{dx} + \frac{\beta}{g} \frac{Q^2}{A^3} \frac{\partial A}{\partial x} \Big|_{h=\text{const}} - \frac{Q^2}{gA^2} \frac{d\beta}{dx}}{1 - \frac{\beta}{g} \frac{Q^2}{A^3} b}, \quad (1)$$

106 where h is the water depth, x is the distance along the main channel in the flow direction, Q is the flow discharge in the
 107 main channel, A and b are the cross-sectional water area and the width at the free surface in the main channel,
 108 respectively, β is the momentum correction coefficient accounting for the expected non-uniform cross-sectional velocity
 109 distribution, V is the lateral outflow velocity norm, φ is the deflection angle of the overflow jet with reference to the
 110 flow direction x , S_0 and S_f are the bottom and friction slopes, respectively, and g is the acceleration due to gravity (see
 111 Fig. 1). The term $(\beta Q^2/gA^3)(\partial A/\partial x)|_{h=\text{const}}$ in the numerator on the right-hand side of Eq. (1) is due to the non-prismatic
 112 geometry of the channel, while the term $(Q^2/gA^2)(d\beta/dx)$ accounts for the longitudinal variation of β along the side weir.

113 If the main channel has a rectangular cross-section with linearly decreasing width along the side weir, the current
 114 channel width b at the streamwise abscissa x (with origin at the downstream end of the weir) can be expressed as
 115 (Hager, 1999):

$$116 \quad b(x) = b_d + \Theta x \quad \text{for } -L \cos \theta \leq x \leq 0, \quad (2)$$

117 with b_d being the width of the main channel downstream of the side weir and Θ the convergence ratio, i.e. the rate of
 118 change of b with x , which is negative for converging channels ($\Theta = -\text{tg}\theta$, being θ the inclination angle of the side weir
 119 with reference to the flow direction x). Accordingly, by introducing the usual simplification that $d\beta/dx = 0$ (e.g., Yen
 120 and Wenzel, 1970), Eq. (1) reduces to

$$121 \quad \frac{dh}{dx} = \frac{S_0 - S_f - \frac{Q}{gA^2} \left(2\beta - \frac{A}{Q} V \cos \varphi \right) \frac{dQ}{dx} + \frac{\beta}{g} \frac{Q^2}{A^3} \Theta h}{1 - \beta \text{Fr}^2}, \quad (3)$$

122 where Fr denotes the Froude number of the flow in the main channel (depending on x along the side weir). For $\Theta = 0$,
 123 Eq. (3) becomes the well-known dynamic equation for gradually varied flow with lateral outflow in prismatic

124 rectangular channels (Chow, 1959; Yen and Wenzel, 1970). On the other hand, by assuming that $V\cos\phi = Q/A$ and
 125 $\beta = 1$, and introducing the further hypothesis that flow diversion does not affect the energy head (De Marchi, 1934) and
 126 thus the specific energy is constant along the side weir ($S_f = S_0$), the following equation can be obtained from Eq. (3):

$$127 \quad \frac{dh}{dx} = \frac{-\frac{Q}{gA^2} \frac{dQ}{dx} + \frac{Q^2}{gA^3} \Theta h}{1 - Fr^2}. \quad (4)$$

128 Eq. (4) can be alternatively derived by adopting the energy approach with the assumption that the specific energy of the
 129 main channel flow is constant throughout the side weir and the Coriolis coefficient α is uniformly equal to one.

130 The differential equation of the flow profile must be coupled with a suitable equation for the computation of the
 131 discharge per unit length overflowing through the weir. The conventional weir formula can be adopted for this purpose,
 132 which, in the present application involving a converging side weir, reads:

$$133 \quad \frac{dQ_w}{dx} = -\frac{dQ}{dx} = C_d \sqrt{2g} (h-w)^{3/2} (1 + \Theta^2)^{1/2}, \quad (5)$$

134 where Q_w is the discharge overflowing through the side weir, C_d is the discharge coefficient, and w is the height of the
 135 weir crest above the bottom of the main channel. Hager (1987) proposed a correction of the outflow equation to include
 136 the effects of the local flow depth, the incoming flow velocity, and the lateral outflow angle.

137 De Marchi (1934) first provided a general analytical solution of the differential problem represented by Eqs. (4) and
 138 (5) in the case of $\Theta = 0$, by assuming a fixed value for C_d . Conversely, for $\Theta \neq 0$, the system of Eqs. (4) and (5) must be
 139 solved numerically. By introducing the following dimensionless quantities:

$$140 \quad \bar{x} = \frac{x}{B}, \quad \bar{h} = \frac{h}{E_0}, \quad \bar{w} = \frac{w}{E_0}, \quad (6)$$

141 with B being the width of the approach channel and E_0 the specific energy of the flow (assumed constant along the
 142 lateral outflow), the equation of the flow profile in a rectangular converging channel can be written in dimensionless
 143 form as follows:

$$144 \quad \frac{d\bar{h}}{d\bar{x}} = \frac{2C_d(\bar{h} - \bar{w})^{3/2}(1 - \bar{h})^{1/2}(1 + \Theta^2)^{1/2} + 2(1 - \bar{h})\Theta\bar{h}}{(1 + \Theta\bar{x})(3\bar{h} - 2)} \quad \text{for } \bar{w} \leq \bar{h} \leq 1, \quad (7)$$

145 in which only the dimensionless parameters C_d , \bar{w} , and Θ appear (Hager, 1999).

146 Hager and Volkart (1986) observed that, for $\Theta < 0$, Eq. (4) admits the theoretical possibility of a pseudo-uniform
 147 flow characterized by invariable flow depth, lateral outflow intensity, and cross-sectional velocity along the converging
 148 channel, despite the decreasing discharge. This special flow state is theoretically obtained when

$$149 \quad -\frac{dQ}{dx} + \frac{Q}{A} \Theta h = 0, \quad (8)$$

150 or in dimensionless form:

151
$$C_d(\bar{h} - \bar{w})^{3/2}(1 + \Theta^2)^{1/2} + (1 - \bar{h})^{1/2}\Theta\bar{h} = 0, \quad (9)$$

152 and can be usefully adopted as a reference design condition in practical applications.

153 Profiles of side weir flow in converging rectangular mild-slope channels can be classified according to the nature of
 154 the flow (subcritical or supercritical) and the sign assumed by the flow parameter which appears in the numerator on the
 155 right-hand side of Eq. (3) or Eq. (4). Accordingly, if the flow is subcritical, the flow profile for $\Theta < 0$ can be a
 156 backwater curve (with increasing water depth in the direction of flow) or a drawdown curve (with decreasing water
 157 depth in the direction of flow), unlike what happens for the case of $\Theta = 0$, in which only increasing flow profiles are
 158 possible. Moreover, the subcritical flow profiles tend upstream to the pseudo-uniform depth line (if this is higher than
 159 the critical one), thereby confirming that converging side weirs can potentially improve the outflow efficiency
 160 compared to conventional ones, where the subcritical profiles tend asymptotically upstream to the weir crest (when it
 161 remains higher than the critical line). A detailed classification of flow profiles based on Eq. (7) is reported in Hager and
 162 Volkart (1986) and Hager (1999) for both subcritical and supercritical flow conditions.

163

164 **Dimensional Analysis**

165 Side weir steady flows in converging rectangular channels can be analyzed effectively by using dimensionless
 166 analysis.

167 Firstly, the following geometric quantities can be selected to describe the geometry of the system (see Fig. 1): the width
 168 of the approach rectangular channel, B ; the width of the main channel downstream of the side weir, b_d ; the height of the
 169 side weir crest above the channel bottom, w ; the length of the weir crest, L ; the thickness of the weir crest, s ; the bottom
 170 slope of the channel, S_0 ; and the roughness coefficient of the channel, ε .

171 Moreover, due to the subcritical state of the flow (which is simultaneously affected by both upstream and
 172 downstream conditions), the physically significant flow variables involved in the problem are: the total overflowing
 173 discharge Q_w ; the discharge of the incoming flow, Q_0 , which can be equivalently substituted by the discharge of the
 174 onward flow $Q_d = Q_0 - Q_w$; the water depth at the downstream end of the side weir, h_d .

175 Finally, the fluid properties affecting the flow are: the mass density, ρ ; the specific weight, γ ; the dynamic viscosity,
 176 μ ; and the surface tension, σ .

177 Therefore, the overflowing discharge can be expressed as a suitable function of the other 13 independent variables
 178 introduced above as follows:

179
$$Q_w = f_1(B, b_d, w, L, s, S_0, \varepsilon, h_d, Q_d, \rho, \gamma, \mu, \sigma). \quad (10)$$

180 By choosing ρ , h_d , and Q_d as scaling variables and neglecting the effect of viscosity and surface tension, the
 181 following dimensionless functional relationship can be derived according to the Π -theorem:

$$182 \quad \eta = f_2 \left(\frac{B-b_d}{L}, \frac{b_d}{h_d}, \frac{w}{h_d}, \frac{L}{h_d}, \frac{s}{h_d}, S_0, \frac{\varepsilon}{h_d}, \frac{Q_d}{h_d^2 \sqrt{gh_d}} \right), \quad (11)$$

183 where $\eta = Q_w/(Q_w+Q_d) = Q_w/Q_0$ is the overflow efficiency, defined as the dimensionless ratio of the spilled discharge Q_w
 184 to the incoming flow discharge Q_0 . A straightforward physical interpretation can be given to the dimensionless
 185 geometric ratios in Eq. (11); in detail (see Fig. 1): $(B-b_d)/L = [\Theta^2/(1+\Theta^2)]^{1/2}$ is a function of the convergence ratio Θ ,
 186 thus is an index of the main channel contraction rate along the side weir; b_d/h_d is a cross-sectional shape parameter; w/h_d
 187 represents a dimensionless crest elevation characteristic of the weir; L/h_d is a dimensionless length of the crest weir; s/h_d
 188 denotes a crest thickness ratio; and ε/h_d is a dimensionless hydraulic factor representing the channel roughness.

189 The last dimensionless term in Eq. (11) is the Froude number Fr_d of the onward flow.

190 The bottom slope parameter S_0 can be disregarded in Eq. (11) in the first approximation (see Borghei et al., 1999),
 191 due to the fact that side weirs are typically designed for subcritical flows and are commonly inserted in mild slope
 192 channels. Moreover, theoretical and experimental studies (e.g. De Marchi, 1934; Gentilini, 1938) have proved that the
 193 flow diversion does not significantly increase the intensity of the dissipative processes which occur in the main channel
 194 flow in uniform conditions, especially for short side weirs. Accordingly, the difference between the bottom and friction
 195 slopes can be neglected in the numerator of the right-hand side of Eq. (3), and the same applies for the assessment of the
 196 outflow efficiency. The dependence on the roughness parameter ε/h_d may then be eliminated from Eq. (11), which
 197 hence becomes:

$$198 \quad \eta = f_3 \left(\Theta, \frac{b_d}{h_d}, \frac{w}{h_d}, \frac{L}{h_d}, \frac{s}{h_d}, Fr_d \right), \quad (12)$$

199 where only 7 dimensionless groups are involved. The same functional relationship can be extended to the discharge
 200 coefficient of Eq. (5):

$$201 \quad C_d = f_4 \left(\Theta, \frac{b_d}{h_d}, \frac{w}{h_d}, \frac{L}{h_d}, \frac{s}{h_d}, Fr_d \right). \quad (13)$$

202 In this paper special attention is devoted to the effect of the non-prismaticity (described by the convergence ratio Θ).
 203 Some values of the dimensionless crest height and various flow conditions (corresponding to different values of Fr_d) are
 204 considered too, whilst the influence of the other geometrical dimensionless parameter is not investigated. It should be
 205 noted that most studies on side weir flows in prismatic channels use dimensionless terms defined on the basis of
 206 upstream flow variables and assume Fr_0 as the key similarity parameter (e.g. Subramanya and Awasthy 1972;
 207 Nandesamoorthy and Thomson 1972; Ranga Raju et al. 1979; Hager 1987; Singh et al., 1994; Jalili and Borghei, 1996;
 208 Borghei et al., 1999; Emiroglu et al., 2011). However, the use of downstream flow variables to define dimensionless
 209 terms is preferred in this work, because the flow profile is controlled by downstream conditions in subcritical flows.
 210 Finally, it is a well-known fact that a different choice of the scaling variables can lead to a different set of dimensionless

211 terms without reducing the overall informative content of the final relationships. In particular, Honar and Javan (2007),
212 and Říha and Zachoval (2014) include suitable ratios between upstream and downstream flow variables in the set of
213 dimensionless groups influencing the discharge coefficient.

214

215 **Laboratory experiments**

216 The experimental investigation was carried out at the Hydraulic Laboratory of the University of Brescia (Italy). The
217 laboratory apparatus and the main features of the experimental tests are described in this section.

218

219 *Experimental set-up*

220 Experiments were performed within an 11 m long, 0.7 m wide, and 0.4 m high tilting flume equipped with a
221 recirculating system (Fig. 2). The flume was hydraulically smooth, with acrylic walls and a stainless steel bottom.
222 Water entered the flume from a large head tank and flowed down freely into a downstream tank at the flume outlet.

223 A longitudinal wall was placed in the flume to obtain two parallel rectangular channels acting as main and lateral
224 spillway channel, respectively. This dividing wall had an intermediate segment arranged obliquely with reference to the
225 sides of the laboratory flume. Thus, an approximately 1.50 m long converging stretch with linearly decreasing width
226 (from 0.36 m to 0.18 m) was obtained in the main channel, at 5.45 m from the flume inlet (see Fig. 2a). A short-crested
227 weir with crest parallel to the channel bottom and adjustable height was inserted in the oblique wall. The crest of the
228 weir was 5.5 cm thick and characterized by rounded entrance. The picture in Fig. 3, taken during a typical experimental
229 test, shows a detail of the laboratory setup including the oblique side weir.

230 The inflow discharge was adjusted through a butterfly valve mounted on the supply pipe. A sluice gate was inserted
231 in the main channel, at 0.61 m from the downstream end of the side weir, in order to regulate the tailwater level. A
232 0.15 m high rectangular thin-plate weir calibrated in the discharge range [1, 15] l/s was also placed at 3.46 m from the
233 downstream end of the side weir to measure the discharge Q_d of the flow proceeding downward in the main channel
234 (Fig. 2). The overflow discharge was then computed by difference once the inflow rate was known.

235 The inflow rate was measured using an electromagnetic ISOMAG flow meter with 0.07 l/s accuracy, flange-mounted
236 on the supply pipe. Water depth measurements were also accomplished by means of 0.5 mm accurate Banner S18U
237 ultrasonic transducers at the observation points indicated in Fig. 4, with the aim of describing the shape of the water
238 surface near the side weir and obtaining both longitudinal and transverse water surface profiles in the main channel.
239 Voltage output signals from the measuring devices were acquired for 2 min in each test condition and sampled at 1 Hz
240 using a DT 9804 data logger with 16 bit resolution. Finally, a Nixon Streamflow miniature velocity meter (equipped
241 with a 15 mm propeller diameter) was employed for a limited set of experimental tests to perform punctual velocity
242 measurements for 1 min at 10^{-1} Hz frequency, with accuracy of 1.5% of the measured value. In this way, velocity

243 distributions at selected cross-sections (Fig. 4) were reconstructed with suitable spatial resolution, and discharge
 244 profiles as well as velocity-head and momentum coefficient profiles along the side weir were obtained. Lateral outflow
 245 angles at selected locations over the crest weir were estimated by combining longitudinal and transverse velocity
 246 measurements.

247

248 *Experimental plan*

249 All experimental tests concerning side weir flows in a non-prismatic channel were carried out by assuming the
 250 dimensionless weir length L/B equal to 4.17 and the contraction ratio b_d/B equal to 0.5 ($L/b_d = 8.33$). Hence, the
 251 inclination θ of the side weir with reference to the flow direction was approximately equal to 7° ($\Theta = -0.12$). This
 252 value of the convergence ratio is quite significant (Honar and Javan, 2007) and realistic for practical applications and, at
 253 the same time, ensures that gradually varied flow conditions occur. The bottom slope of the channel was set to zero.

254 Table 1 shows the experimental conditions of the 40 steady flows investigated, characterized by different weir
 255 heights ($w = 0.203$ m, 0.183 m, or 0.153 m), inflow rates (ranging approximately from 20 to 60 l/s), and tailwater
 256 conditions (induced by different heights of the downstream sluice gate opening). The upstream Froude number Fr_0 lies
 257 in the range $[0.15, 0.45]$, which is comparable to the one considered by Honar and Javan (2007) for a similar
 258 convergence ratio. Accordingly, the flow was always significantly subcritical and a weir efficiency η ranging
 259 approximately between 0.59 and 0.95 was achieved. All experiments were performed in free overflow conditions with
 260 fully ventilated nappe. Moreover, a sufficiently high water head above the weir crest was ensured to minimize the effect
 261 of surface tension. According to the theoretical analysis of Section 2, two different types of flow profiles (increasing or
 262 decreasing in the flow direction) are possible in the range of \bar{w} here considered (0.67-0.86), depending on the
 263 downstream boundary condition. However, in the investigation presented here only rising flow profiles were observed,
 264 mainly due to the strong backwater effect caused by the presence of control and measuring devices in the main channel
 265 downstream of the side weir. For reasons of outflow efficiency, this is actually the most interesting situation in practical
 266 applications.

267 Experimental water surface profiles were acquired in all tests by measuring the water depth along the channel
 268 centerline at the point gauges located at $x = -1.75, -1.55, -1.35, -1.15, -0.95, -0.75, -0.55, -0.35, -0.15, 0.05, 0.25$ m,
 269 being x the streamwise coordinate originating from the side weir end (see Fig. 4). Based on this information, an average
 270 value of the discharge coefficient C_d in Eq. (5) was computed for each experimental test according to the following
 271 definition (Gentilini, 1938):

$$272 \quad \bar{C}_d = \frac{Q_w}{\sqrt{2g} \int_0^L (h-w)^{3/2} dl} \cong \frac{Q_w}{\sqrt{2g} \sum_i (h_i - w)^{3/2} \Delta l_i}, \quad (14)$$

273 in which, by assuming the side weir as being discretized according to the stencil of Fig. 4 , Δl_i is the length of the i -th
274 stretch ($\sum_i \Delta l_i = L$), and $h_i - w$ is the corresponding water head above the weir crest (Tab. 1).

275 The main characteristics of the flows of Tests N15 and N40 (marked with a star superscript in Tab. 1) were analyzed
276 in further detail since they are characterized by fairly different values of Fr_0 and w/h_d in the ranges investigated. During
277 Tests N15 and N40, transverse water surface profiles (in the y -direction) were measured at selected cross-sections (I,
278 III, IV, VI, VIII, IX, and XI in Fig. 4) based on 6 water level gauge points located at different transverse distances from
279 the lateral side. Moreover, the water surface elevation above the weir crest was measured at 7 gauge points (along
280 profile g at sections from III to IX in Fig. 4). Finally, velocity measurements were carried out to investigate the side
281 weir effect on the cross-sectional distribution of the longitudinal velocity along the main channel. For each selected
282 cross-section (I, III, IV, VI, VIII, IX, and XI in Fig. 4), 7 vertical velocity profiles were acquired, each of which
283 described by 6 measuring points (see Fig. 6 for an example of a stencil of velocity gauge points over a cross-section).

284 A set of 31 experimental tests of flow over conventional side weirs was carried out in the same laboratory facility
285 described above to assess the improvement in outflow efficiency induced by the converging side weir. To this purpose,
286 the approach channel width B was reduced at 0.18 m and a 1.5 m-long short-crested one-side weir with adjustable crest
287 height was inserted in the flume ($L/B = 8.33$). The test conditions are summarized in Table 2 and are characterized by
288 different weir crest heights (w ranges from 0.203 m to 0.120 m for five positions) and different values of the inflow
289 discharge. The downstream sluice gate was not operated in this series of experimental tests and did not interfere with
290 the flow. Hence, the tailwater flow depth was essentially controlled by the rectangular sharp-crested weir in the onward
291 flow channel. The tests marked with a star superscript in Tab. 2 (Tests P9, P13, and P18) were further investigated by
292 performing accurate measurements of longitudinal and transverse free surface profiles, as well as of cross-sectional
293 velocity distributions, as described above. In this set of experimental tests the discharge of the incoming flow varies
294 between 8 and 25 l/s, with weir efficiency ranging from 0.40 to 0.96. The upstream Froude number lies in the range
295 [0.18, 0.59] in the experimental tests characterized by $w = 0.203$ m, 0.183 m, and 0.153 m; higher values of Fr_0 (up to
296 0.82) are obtained for lower values of w ($w = 0.133$ m, and 0.120 m).

297

298 **Analysis of results**

299 In this section experimental results are presented and analyzed in order to describe the main features of the side weir
300 flow and find the dimensionless parameters which mainly influence diversion capacity.

301

302 ***Flow characteristics***

303 Fig. 5 shows the shape of the measured water surface for a typical experimental test (Test N15) concerning a
304 subcritical side weir flow in a converging channel. The longitudinal profiles measured along both the channel centerline

305 and the weir side of the main channel (Fig. 5a) have a characteristic rising curved shape, which is typical of backwater-
 306 type profiles. Entrance effects triggered by the lateral outflow induce a slight drop in the water surface at the upstream
 307 end of the side weir (see, for example, Emiroglu et al., 2011), which is more accentuated near the upstream corner of
 308 the weir (Fig. 5d). For all the experimental tests of Tab. 1, the water depth measured at the downstream end of the side
 309 weir is higher than the upstream one; experimental data show that the relative difference between the water depths at the
 310 two ends of the side weir (computed with reference to the upstream water depth h_0) increases with the Froude number
 311 of the incoming flow (for $0.16 \leq Fr_0 \leq 0.46$). Moreover, overflow causes an expected transverse drawdown effect on the
 312 water surface (e.g. Muslu et al., 2003), as clearly shown by the transverse water surface profiles reported in Figs. 5b and
 313 c. The transverse drop in water surface elevation between the channel centerline and the weir side is in the order of 2%
 314 for Test N15, and increases slightly moving downwards along the side weir. The transverse inclination of the water
 315 surface is therefore small, except for the flow region immediately close to the weir.

316 Lateral outflow is expected to affect the cross-sectional velocity distribution in the main channel along the weir. Fig.
 317 6 shows the general pattern of the longitudinal velocity u in Section VI for Test N15 as a typical example: the contour
 318 map of the measured longitudinal velocities (in the x -direction), adimensionalized with the corresponding cross-
 319 sectional average velocity U , is represented together with some vertical and horizontal velocity profiles; the average
 320 velocity U is estimated by the formula:

$$321 \quad U = \frac{\sum u \Delta A}{\sum \Delta A}, \quad (15)$$

322 where the longitudinal velocity u measured at the grid nodes shown in Fig. 6 is multiplied for the corresponding area of
 323 influence ΔA defined using the Thiessen polygon method. Lateral overflow causes the zone of highest longitudinal
 324 velocities to shift towards the weir side of the channel and the maximum value of the longitudinal velocity can be found
 325 just below the weir crest. This asymmetrical pattern had already been observed by El-Khashab and Smith (1976) for
 326 conventional side weirs. The combined effect of the inclined side of the flume and of the drawdown caused by the water
 327 drop accelerates the flow on the weir side of the channel compared to the flow on the wall side (compare vertical
 328 profiles 5, 6, and 7 with profiles 1, 2, and 3 in Fig. 6). Consequently, vertical and horizontal velocity profiles are
 329 sensibly curved.

330 Figs. 7a and b illustrate contours of equal longitudinal velocity for Test N15 near the channel bottom and near the
 331 water surface (levels A and F, respectively; see Fig. 6). The horizontal sections of the longitudinal velocity close to the
 332 free surface show that because of the lateral outflow the maximum velocity moves progressively towards the weir crest.
 333 This deflection of the flow velocity distribution is in agreement with the experimental observations of Michelazzo et al.
 334 (2015) on side weirs with zero-height crest in a prismatic channel. Conversely, close to the bottom, due to the zero-
 335 velocity condition at the lateral walls, the maximum velocity occurs approximately at the centerline of the channel. This

336 induces an overall distortion of the cross-section velocity distribution. The profiles of flow discharge in the main
 337 channel can be obtained by integrating the experimental velocity distributions at each measuring cross-section via the
 338 classic velocity-area method (e.g. Corbett et al., 1943); the profiles of outflow discharge along the side weir can be then
 339 derived by difference (see Fig. 8 for Test N15). It should be observed that the flow discharges obtained at cross-sections
 340 I and XI agree with the measures provided by the electromagnetic flow meter and the normal rectangular thin-plate
 341 weir, respectively, with an absolute deviation in the order of 10^{-1} l/s (which corresponds to a relative error in the order
 342 of 1%). Moreover, Fig. 8 compares the profile of the dimensionless channel discharge along the side weir with the
 343 analogous profiles concerning six horizontal strips (corresponding to successive levels A, B, C, D, E, and F above the
 344 channel bottom) in which the channel flow can be vertically divided. The channel discharge is adimensionalized by the
 345 inflow discharge Q_0 , while the flow discharge through each horizontal strip is adimensionalized by the discharge
 346 measured at section I for the same strip. The profiles of the strips located at deeper levels drop more rapidly, revealing
 347 that lateral cross-sectional currents develop and progressively strengthen downward along the side weir. These lateral
 348 currents can be expected to noticeably influence the overall flow dynamics.

349 Due to the non-uniform distribution of longitudinal velocity over the cross-sections of a weir flow, the usual
 350 velocity-distribution coefficients could reach values significantly higher than 1 (e.g. Michelazzo et al., 2015) and can be
 351 expected to vary quite rapidly from section to section in the direction of flow, thus questioning the validity of the
 352 common approximation of omitting both β and $d\beta/dx$ in Eq. (1). The analysis of the experimental velocity data acquired
 353 for Tests N15 and N40 highlights that both the velocity-head and momentum coefficients (α and β , respectively)
 354 increase along the side weir (see Tab. 3). The coefficients α and β are slightly higher than unity in the incoming flow
 355 and in the first stretch of the weir flow, growing almost up to 2 and 1.3, respectively, at the downstream end of the weir
 356 in Test N40. Although the data set is limited, experimental data consistently suggest that, for fixed Θ , α and β are well
 357 correlated to the local outflow efficiency η_l , defined as the ratio between the cumulative discharge overflowed up to the
 358 current cross-section and the discharge of the incoming flow (Fig. 9). Both α and β increase with η_l and can be well
 359 estimated through a polynomial function of fifth order for $\Theta = -0.12$ and of second order for $\Theta = 0$. The non-
 360 prismaticity of the main channel produces the effect of reducing the values of the velocity-distribution coefficients for
 361 fixed η_l , in comparison with the conventional side weir flow in a prismatic channel. Actually, the gradual channel
 362 contraction along the side weir can be expected to hinder the development of tree-dimensional flow structures (due to
 363 the occurrence of spiral motion or flow separation, for example), thus promoting a more uniform cross-sectional
 364 distribution of the longitudinal velocity compared to the one occurring in a prismatic channel with equal weir
 365 efficiency. Furthermore, Tab. 3 compares the values of the computed quantities $(1/A)(\partial A/\partial x)|_{h=\text{const}}$ and $(-1/\beta)(d\beta/dx)$
 366 along the side weir for Tests N15 and N40. Both these factors multiply the same quantity $(\beta Q^2)/(gA^2)$ in the two last

367 terms of the numerator of Eq. (1). Due to the simple geometry of the converging channel, $(1/A)(\partial A/\partial x)|_{h=\text{const}}$ is equal to
368 Θ/b , hence is a purely geometric x -dependent factor, which is independent of the specific test condition. It should be
369 noted that the absolute values of both these factors increase along the weir and that the term $(-1/\beta)(d\beta/dx)$, which is
370 negligible compared to $(1/A)(\partial A/\partial x)|_{h=\text{const}}$ in the upstream portion of the side weir flow, becomes comparable to it when
371 approaching the downstream end of the weir. Therefore, whenever the outflow efficiency of the weir is high, a priori
372 one could expect that the omission of the term $(-1/\beta)(d\beta/dx)$ in Eq. (1) is questionable, especially near the downstream
373 end of the weir. However, the actual consequences of this approximation are practically negligible, as will be shown in
374 the following. Finally, Tab. 3 shows that even in the case of side weirs inserted in non-prismatic channels the lateral
375 outflow angle φ gradually increases along the side weir, as already observed in conventional lateral outflows in
376 prismatic channels (e.g. Hager, 1987).

377 A check of the validity of the usual basic assumption that the energy line is parallel to the bottom is performed in
378 Fig. 10, in which, for all tests reported in Tab. 1, the experimental ratio between the total head at the upstream and
379 downstream ends of the side weir (Sections I and XI, respectively) is plotted against the upstream Froude number. The
380 velocity heads at the two extremities of the weir are assessed by estimating the energy coefficient α according to the
381 fifth-order polynomial regression of the data of Tests N15 and N40 represented in Fig. 9a. The absolute average relative
382 difference between the specific energy upstream and downstream of the weir (with reference to the downstream one) is
383 0.48%. Negative differences occurring in some cases ($E_0/E_d < 1$ in Fig. 10) are attributable to inaccuracies in water
384 depth and discharge measurements. In particular, in Test N15 the experimental total head profile computed from water
385 depth and velocity-distribution measurements shows an overall variation comparable with the accuracy of the water
386 depth measurement (approximately 1 mm), while for Test N40 a total head loss of 4 mm (corresponding to 1.80% of the
387 total energy at the upstream end of the side weir) can be assessed from the experimental data. The maximum relative
388 difference between upstream and downstream energy is observed for Test N39 (for which the upstream Froude number
389 assumes the maximum value in the range considered) and is equal to 1.89%. For the set of experimental tests performed
390 in a prismatic channel (Tab. 2), the average value of the specific energy difference between the two ends of the weir is
391 in the order of 2%, which is comparable with experimental results obtained by other authors (e.g. El-Khashab and
392 Smith, 1976; Borghei et al., 1999; Borghei and Parvaneh, 2011). Therefore, it can be concluded that the specific energy
393 of the main channel flow along the side weir is slightly affected by the spill flow process, even in the case of a non-
394 prismatic converging channel, especially for low Froude number conditions ($Fr_0 < 0.35$).

395

396 ***Outflow efficiency***

397 Fig. 11a plots the experimental data concerning both the converging and conventional side weir in the plane $Fr_d - \eta$,
 398 providing a graphical representation of the empirical correlation of η versus Fr_d (in the range $0 \leq Fr_d \leq 0.2$) for different
 399 values of w/h_d . For a fixed value of w/h_d , overall outflow efficiency η decreases as Fr_d increases. Similarly, for an
 400 assigned value of Fr_d , outflow efficiency decreases as w/h_d grows; this last trend is less pronounced for lower values of
 401 Fr_d .

402 The improvement in outflow efficiency induced by the non-prismaticity of the main channel can be assessed from
 403 Fig. 11a. Indeed, for fixed values Fr_d and w/h_d , outflow efficiency is systematically greater for the converging side weir
 404 flow ($\Theta = -0.12$) than for the conventional one ($\Theta = 0$). This effect becomes more significant with growing values of
 405 Fr_d .

406 Furthermore, the analysis of the experimental data suggests that outflow efficiency η can be effectively correlated to
 407 the only dimensionless ratio $\chi = (1/Fr_d)/(w/h_d)$ according to the rational regression function:

$$408 \quad \eta = 1 - \frac{1}{c\chi^\alpha}, \quad (16)$$

409 where c and α are two parameters of the regression model. Best fitting based on the least square method provides
 410 $c = 0.6155$ and $\alpha = 0.8180$ for the converging side weir with $\Theta = -0.12$, $L/B = 4.17$, and $L/b_d = 8.33$ (Fig. 11b). The root
 411 mean square error is equal to 3.9%. Predicted and measured values of outflow efficiency are compared in Fig. 11c. The
 412 difference between estimated and experimental data is less than 10% in 95% of the cases. The average percent error of
 413 the regression model is equal to 3.5%.

414 As for side weir flow in a prismatic channel ($\Theta = 0$, $L/B = 8.33$), from the regression analysis of the experimental
 415 data set based on the same regression function of Eq. (16) it can be obtained that $c = 0.1424$ and $\alpha = 1.2319$, with a
 416 6.3% root mean square error (Fig. 11b). The average percent deviation between experimental and predicted data is
 417 equal to 7.4%; 6 data points out of 31 show a percent deviation greater than 10% (Fig. 11c). Therefore, the converging
 418 side weir appears more efficient than the conventional one for $\chi < 30$ approximately (Fig. 11b), and the improvement in
 419 efficiency grows for lower values of χ . Conversely, the performances of the two devices are practically equivalent for
 420 $\chi > 30$. This is a consequence of the fact that growing values of χ are related to progressively lower values of either Fr_d
 421 or w/h_d . Both these conditions act in the direction of reducing the dynamic effect induced by the converging wall of the
 422 channel.

423

424 *Discharge coefficient*

425 Eq. (13) suggests the dependence of the average discharge coefficient \bar{C}_d on 6 dimensionless groups, but only the
 426 dependence on Θ , w/h_d , and Fr_d is explored here.

427 Depending on the scaling variables, the upstream Froude number Fr_0 can be introduced in Eq. (13) in place of Fr_d .
428 Several empirical formulas have been proposed in literature to estimate the discharge coefficient of a side weir flow in a
429 prismatic channel involving Fr_0 only (e.g. Subramanya and Awasthy, 1972; Hager, 1987). Accordingly, Fig. 12 plots
430 the average discharge coefficient \bar{C}_d against Fr_d (Fig. 12a) and Fr_0 (Fig. 12b) for both the experimental data sets
431 concerning the converging channel with $\Theta = -0.12$ and the prismatic channel ($\Theta = 0$). The scatter of the data in Fig. 12a
432 and b proves that also other parameters influence the discharge coefficient sensibly in addition to either Fr_d or Fr_0
433 (Borghai et al., 1999; Emiroglu et al., 2011). In any case, with regard to side weir flows in a converging channel, the
434 measured values of \bar{C}_d lie in the range $[0.36, 0.46]$ for $Fr_d \leq 0.17$ and $Fr_0 \leq 0.45$, and show a slightly increasing trend
435 with both Fr_d and Fr_0 .

436 In order to better represent data correlations, Fig. 12c plots the dimensionless group $\bar{C}_d / (w/h_d)^2$ as a function of Fr_0
437 for given Θ . The two sets of experimental data (for $\Theta = -0.12$ and $\Theta = 0$, respectively) seem to converge for Fr_0
438 approaching zero, when Θ is reasonably expected not to be influential on \bar{C}_d . Moreover, each can be interpolated by a
439 linear regression function with rate of change depending on the convergence rate Θ . Experimental data show that
440 converging side weirs provide higher values of \bar{C}_d compared with the conventional ones for fixed values of Fr_0 and
441 w/h_d , and confirm that \bar{C}_d tends to increase with increasing values of Fr_0 for fixed w/h_d and Θ (Fig. 12c). The latter
442 trend agrees with the observations of Emiroglu et al. (2011), which highlighted that in conventional side weirs the
443 discharge coefficient increases together with the upstream Froude number when $L/b_d > 1$ (such as in the present study,
444 in which $L/b_d = 8.33$), whereas the opposite occurs for lower values of L/b_d (see, for example, Subramanya and
445 Awasthy, 1972; Ranga Raju et al., 1979; Singh et al., 1994; Borghai et al., 1999). This may be explained by the fact that
446 the strength of the secondary flows caused by the lateral diversion actually grows as the upstream Froude number
447 increases. Finally, the effect of Θ on the discharge coefficient may be ascribed to the fact that, due to the oblique
448 arrangement of the side weir, the incoming flow acquires a velocity component normal to the weir crest which
449 facilitates the diversion process.

450

451 ***Effectiveness of one-dimensional modeling***

452 As the 1D modeling approach is typically adopted in literature to predict the main engineering aspects of spatially
453 varied flows due to lateral outflow (e.g. Chow, 1959; Hager, 1999), the effectiveness of this approach in the case of a
454 converging channel is checked in this subsection based on the data obtained from the experimental tests.

455 With this aim, Eqs. (1) and (5) are numerically solved through the classic fourth-order Runge-Kutta method by
456 adopting the hypotheses that $V_{\cos\phi}$ is equal to the local cross-sectional velocity U and that C_d is uniform along the weir

457 and equal to the average value \bar{C}_d calculated from the experimental data according to Eq. (14). To assess the effect of
 458 the term $(-1/\beta)(d\beta/dx)$ on the numerical solution of Eq. (1), the computations are performed both assuming $\beta = 1$ along
 459 the side weir and β dependent on x according to a suitable regression model based on the experimental data reported in
 460 Tab. 3. Water depth and flow rate values measured at the downstream end of the side weir are imposed as downstream
 461 boundary conditions for the computation of water depth and flow discharge profiles in subcritical flow regime.

462 Fig. 13 shows the comparison between experimental data and numerical results (obtained with a uniform spatial
 463 discretization of size $\Delta x = 10^{-3}$ m) for Tests N15 ($\bar{C}_d = 0.410$) and N40 ($\bar{C}_d = 0.388$). Moreover, Fig. 13 compares
 464 numerical profiles computed by setting $\beta = 1$ with the ones obtained by considering the longitudinal variability of β
 465 along the weir. The numerical profiles of both water surface and flow discharge agree fairly well with the experimental
 466 ones, especially for Test N15. In Test N40 both profiles are slightly underestimated, as well as the overall discharge
 467 diverted laterally; however, the total water depth variation along the side weir is well predicted. The discrepancies
 468 observed in Test N40 are probably due to two main reasons, i.e. presumably high variability of the discharge coefficient
 469 along the weir, and the effect of strong secondary cross currents (and the accompanying turbulence) induced by the
 470 considerable intensity of the lateral outflow. The latter effect cannot be thoroughly included in the numerical model by a
 471 simple variation of β along the side weir flow. Fig. 13 shows that the inclusion in the model of the variability of β along
 472 the side weir does not substantially improve the accuracy of the numerical prediction. To confirm this observation, the
 473 global error between experimental and numerical profiles is computed using the standard discrete 1-norm of relative
 474 deviations, defined as:

$$475 \quad E_h = \sum_{i=1}^{n_h} \left| \frac{h_{i,num} - h_{i,exp}}{h_{i,exp}} \right|, \quad E_Q = \sum_{i=1}^{n_Q} \left| \frac{Q_{i,num} - Q_{i,exp}}{Q_{i,exp}} \right| \quad (17)$$

476 for water depth and flow discharge profiles, respectively. In Eq. (17) the index i refers to a current measuring point
 477 where experimental data are available, while n_h and n_Q indicate the total number of measuring points of h and Q ,
 478 respectively, along the side weir. The results are reported in Table 4.

479 The pseudo-uniform flow is a theoretical side weir flow condition potentially induced by the converging geometry of
 480 the main channel, and is characterized by uniform lateral outflow intensity and channel velocity, as explained in a
 481 previous section. An additional ad hoc experimental test was devised with $\Theta = -0.12$ and $\bar{w} = 0.872$ to verify the
 482 occurrence of this theoretical flow condition. The test is characterized by: $w = 0.203$ m, $Q_0 = 19.54$ l/s, $Fr_0 = 0.158$,
 483 $Q_d = 7.90$ l/s, $Fr_d = 0.126$, $Q_w = 11.64$ l/s, $\eta = 0.596$; the dimensionless ratio χ is approximately equal to 9, thus a
 484 considerable improvement in outflow efficiency is expected in comparison with the conventional side weir (Fig. 11b),
 485 which confirms the practical interest of this special flow condition. The experimental average discharge coefficient

486 computed according to Eq. (14) is equal to 0.391. Consequently, a theoretical value of 0.229 m derives for the pseudo-
487 uniform water depth by inserting this value for C_d in Eq. (9).

488 Fig. 14 compares theoretical, numerical, and experimental free surface profiles. The numerical profile is computed
489 assuming $\beta = 1$ in order to perform a consistent comparison with the theoretical solution deriving from Eq. (9).
490 Measured profiles a (along the side wall), c (along the main channel centerline), and f (along the weir side) show that
491 the experimental water surface is almost parallel to the bottom, thus the observed flow actually resembles a pseudo-
492 uniform flow. The 1D numerical model predicts the difference in water depth elevation along the side weir to be
493 approximately 1 mm and provides a water surface profile in good agreement with both the theoretical and experimental
494 ones. However, it slightly overestimates both the measured (11.64 l/s) and the theoretical (10.91 l/s) total outflow
495 discharge with a relative error of approximately 4% and 11%, respectively.

496

497 **Conclusions**

498 Lateral side weirs are fundamental hydraulic structures in many civil and agricultural applications, and their
499 importance is demonstrated by the huge scientific and technical literature devoted to the topic. Although side weirs in
500 converging channels exhibit several interesting features and represent effective lateral overflow devices for practical use
501 in diverting flow systems, their analysis has been relatively overlooked in literature. This paper provides a contribution
502 in this direction, based on a wide set of experiments accomplished under subcritical flow conditions in a laboratory
503 flume where a side weir was inserted in a converging channel on its oblique side. The experimental data achieved in a
504 convergent channel with convergence ratio Θ equal to -0.12 are critically compared with the ones obtained from a set
505 of tests performed in a prismatic channel ($\Theta = 0$). Different test conditions are considered, characterized by the
506 upstream Froude number Fr_0 and the dimensionless weir height w/h_d lying in the intervals $[0.15, 0.45]$ and $[0.67, 0.86]$,
507 respectively, while the dimensionless weir length parameter L/b_d is maintained equal to 8.33. The measured weir
508 efficiency η ranges approximately between 0.59 and 0.95.

509 The following main conclusions can be drawn from the analysis carried out in this paper.

510 (1) Due to the lateral outflow, the cross-sectional velocity distribution becomes strongly asymmetrical and the region
511 of highest longitudinal velocities moves towards the weir side of the channel.

512 (2) The two velocity-distribution coefficients α and β are considerably affected by the lateral outflow. Their values
513 typically increase along the side weir in the direction of flow and can be positively correlated to the local outflow
514 efficiency. Values of the coefficients for energy and momentum up to 2 and 1.3, respectively, have been observed. Both
515 velocity-distribution coefficients increase with the local outflow efficiency, with a rate of change which is higher for
516 side weir flows in prismatic channels compared to side weir flows in converging channels. The experimental data show

517 that, in the test conditions explored, the usual approximation of omitting the term accounting for the rate of change of β
518 in the equation of the flow profile leads to a negligible error.

519 (3) The basic constant energy assumption usually adopted in side weir flow modeling is acceptable even for side weir
520 flows in converging channels, especially for low values of the approach Froude number ($Fr_0 < 0.35$). The average value
521 of the absolute relative difference observed between the specific energy upstream and downstream of the side weir is
522 0.48%.

523 (4) Experimental data indicate that Fr_d and w/h_d are relevant dimensionless variables for the description of the overall
524 outflow efficiency parameter η , and that η decreases with the increase of both Fr_d and w/h_d . The non-prismaticity of the
525 main channel improves the outflow efficiency for fixed values of Fr_d and w/h_d . Furthermore, the analysis of the
526 experimental data suggests that η can be suitably correlated to the only dimensionless ratio $\chi = (1/Fr_d)/(w/h_d)$ according
527 to a rational regression function.

528 (5) Measured values of the average discharge coefficient \bar{C}_d for the converging side weir flows considered lie in the
529 range [0.36, 0.46] for $Fr_0 \leq 0.45$ and $Fr_d \leq 0.17$, and show a slightly increasing trend together with both Fr_0 and Fr_d .
530 Moreover \bar{C}_d is significantly influenced by the convergence ratio Θ for fixed values of Fr_0 and w/h_d .

531 (6) The comparison between experimental data and numerical results shows that the 1D modeling approach can
532 predict the main hydraulic characteristics of side weir flows in converging channels.

533 The results confirm that a side weir in a converging channel can improve outflow efficiency compared to a
534 conventional side weir in a prismatic channel for similar flow conditions.

535

536 **Acknowledgement**

537 The Associate Editor and the reviewers are kindly acknowledged for their valuable comments which have greatly
538 contributed to the improvement of the paper.

539

540

541 **References**

542 Aghayari, F., Honar, T., and Keshavarzi, A. (2009). "A study of spatial variation of discharge coefficient in broad-
543 crested inclined side weirs." *Irrig. Drain.*, 58(2), 246–254.

544 Borghei, S. M., Jalili, M. R., and Ghodsian, M. (1999). "Discharge coefficient for sharp-crested side weir in subcritical
545 flow." *J. Hydraul. Eng.*, 125(10), 1051–1056.

546 Borghei, S. M., and Parvaneh, A. (2011). "Discharge characteristics of a modified oblique side weir in subcritical flow."
547 *Flow Meas. Instrum.*, 22(5), 370–376.

- 548 Castro-Orgaz, O., and Hager, W. H. (2012). "Subcritical side-weir flow at high lateral discharge." *J. Hydraul. Eng.*,
549 138(9), 777–787.
- 550 Chow, V. T. (1959). *Open-channel hydraulics*, McGraw-Hill, Singapore.
- 551 Citrini, D. (1942). "Canali rettangolari con portata e larghezza gradualmente variabili [Rectangular channels with
552 gradually varied discharge and width]." *Energ. Elettr.*, 19(5), 254–262; 19(6), 297–301 (in Italian).
- 553 Corbett, D. M., and others (1943). *Stream-gaging procedure*, U. S. Geological Survey, Water-Supply Paper 888.
- 554 Cunge, J. A., Holly, F. M., and Verwey, A. (1980). *Practical aspects of computational river hydraulics*, Pitman,
555 London.
- 556 De Marchi, G. (1934). "Saggio di teoria del funzionamento degli stramazzi laterali [Theory on side weir flows]." *Energ.*
557 *Elettr.*, 12(11), 849–860 (in Italian).
- 558 El-Khashab, A., and Smith, V. H. (1976). "Experimental investigation of flow over side weirs." *J. Hydraul. Div.*,
559 102(HY9), 1255–1268.
- 560 Emiroglu, M. E., Kaya, N., and Agaccioglu, H. (2010). "Discharge capacity of labyrinth side weir located on a straight
561 channel." *J. Irrig. Drain. Eng.*, 136(1), 37–46.
- 562 Emiroglu, M. E., Agaccioglu, H., and Kaya, N. (2011). "Discharging capacity of rectangular side weir in straight open
563 channels." *Flow Meas. Instrum.*, 22(4), 319–330.
- 564 Gentilini, B. (1938). "Ricerche sperimentali sugli sfioratori longitudinali [Experimental investigations on side weirs]." *Energ. Elettr.*, 15(9), 583–595 (in Italian).
- 565
- 566 Gissonni, C., and Hager, W. H. (1997). "Short sewer sideweir." *J. Irrig. Drain. Eng.*, 123(5), 354–363.
- 567 Haddadi, H., and Rahimpour, M. (2012). "A discharge coefficient for a trapezoidal broad-crested side weir in
568 subcritical flow." *Flow Meas. Instrum.*, 26, 63–67.
- 569 Hager, W. H., and Volkart, P. U. (1986). "Distribution channels." *J. Hydraul. Eng.*, 112(10), 935–952.
- 570 Hager, W. H. (1987). "Lateral outflow over side weirs." *J. Hydraul. Eng.*, 113(4), 491–504.
- 571 Hager, W. H. (1999). *Wastewater hydraulics. Theory and Practice*, Springer-Verlag, Berlin.
- 572 Honar, T., and Javan, M. (2007). "Discharge coefficient in oblique side weirs." *Iran Agr. Res.*, 25(2), 27–35.
- 573 Kouchakzadeh, S., and Vatankhah Mohammad-Abadi, A. R. (2002). "Spatially varied flow in non-prismatic channels.
574 I: dynamic equation." *Irrig. Drain.*, 51, 41–50.
- 575 Jalili, M. R., and Borghei, S. M. (1996). "Discussion of "Discharge coefficient of rectangular side weirs" by R. Singh,
576 D. Manivannan, and T. Satyanarayana." *J. Irrig. Drain. Eng.*, 122(2), 132.
- 577 Michelazzo, G., Oumeraci, H., and Paris, E. (2015). "Laboratory study on 3D flow structures induced by zero-height
578 side weir and implications for 1D modeling." *J. Hydraul. Eng.*, 141(10), 04015023.

579 Muslu, Y., Tozlu, H., and Yüksel, E. (2003). "Effect of lateral water surface profile on side weir discharge." *J. Irrig.*
580 *Drain. Eng.*, 129(5), 371–375.

581 Nandesamoorthy, T., and Thomson, A. (1972). "Discussion of "Spatially varied flow over side-weirs" by K.
582 Subramanya, and S. C. Awasthy." *J. Hydraul. Div.*, 98(HY12), 2234–2235.

583 Novak, G., Kozelj, D., Steinman, F., and Bajcar, T. (2013). "Study of flow at side weir in narrow flume using
584 visualization techniques." *Flow Meas. Instrum.*, 29, 45–51.

585 Parvaneh, A., Borghei, S. M., and Jalili Ghazizadeh, M. R. (2011). "Discussion of "Discharge capacity of labyrinth side
586 weir located on a straight channel" by M. E. Emiroglu, N. Kaya, and H. Agaccioglu." *J. Irrig. Drain. Eng.*, 137(11),
587 743–745.

588 Parvaneh, A., Borghei, S. M., and Jalili Ghazizadeh, M. R. (2012). "Hydraulic performance of asymmetric labyrinth
589 side weirs located on a straight channel." *J. Irrig. Drain. Eng.*, 138(8), 766–772.

590 Pilotti, M., Maranzoni, A., Tomirotti, M., and Valerio, G. (2011). 1923 Gleno dam break: case study and numerical
591 modeling. *J. Hydraul. Eng.*, 137(4), 480–492.

592 Ramamurthy, A. S., and Carballada, L. B. (1980). "Lateral weir flow model." *J. Hydraul. Div.*, 106(IR1), Paper 15285,
593 9–25.

594 Ranga Raju, K. G., Gupta, S. K., and Prasad, B. (1979). "Side weir in rectangular channel." *J. Hydraul. Div.*, 105(5),
595 547–554.

596 Řiha, J., and Zachoval, Z. (2014). "Discharge coefficient of a trapezoidal broad-crested side weir for low approach
597 Froude numbers." *J. Hydraul. Eng.*, 140(8), 06014013.

598 Singh, R., Manivannan, D., and Satyanarayana, T. (1994). "Discharge coefficient of rectangular side weirs." *J. Irrig.*
599 *Drain. Eng.*, 120(4), 814–819.

600 Subramanya, K., and Awasthy, S. C. (1972). "Spatially varied flow over side weirs." *J. Hydraul. Div.*, 98(HY1), Paper
601 8627, 1–10.

602 Swamee, P. K., Pathak, S. K., Mohan, M., Agrawal, S. K., and Ali, M. S. (1994). "Subcritical flow over rectangular side
603 weir." *J. Irrig. Drain. Eng.*, 120(1), 212–217.

604 Ura, M., Kita, Y., Akiyama, J., Moriyama, H., and Jha, A. K. (2001). "Discharge coefficient of oblique side-weirs." *J.*
605 *Hydrosci. Hydraul. Eng.*, 19(1), 85–96.

606 Uyumaz, A. (1997). "Side weir in U-shaped channels." *J. Hydraul. Eng.*, 123(7), 639–646.

607 Yen, B. C., and Wenzel, H. G. (1970). "Dynamic equations for steady spatially varied flow." *J. Hydraul. Div.*,
608 96(HY3), 801–814.

609

610 **List of figure captions**

611 **Figure 1** – Definition sketch of the lateral outflow over a one-side weir in a non-prismatic rectangular channel: a)
612 longitudinal section along the weir; b) plane view; c) cross-section at the weir.

613 **Figure 2** – Sketch of the experimental facility: a) plan view; b) longitudinal section (measures in m).

614 **Figure 3** – Detail of the laboratory setup: upstream view of the converging short-crested side weir.

615 **Figure 4** – Location of the gauge points (black spots) for the measurement of longitudinal and transverse water surface
616 profiles: a) prismatic channel; b) converging channel (measures in m).

617 **Figure 5** – Typical measured water surface profiles (Test N15): a) along the channel centerline and the weir side of the
618 main channel (longitudinal section lines c and f , respectively); b) along cross-section line VI; c) along cross-section line
619 IX (z denotes the elevation above the channel bottom). d) Plane contour map of experimental water depth in the
620 converging channel (contour labels in cm).

621 **Figure 6** – Typical distribution of dimensionless longitudinal velocity in a cross-section along the converging channel
622 (Section VI, Test N15) for subcritical flow conditions; U is the computed cross-sectional average velocity. Velocity
623 contour levels are derived by interpolation from measurements performed at bold crosses.

624 **Figure 7** – Typical contour maps of experimental longitudinal velocities along the side weir (Test N15): a) bottom
625 flow; b) surface flow (contour labels in m/s).

626 **Figure 8** – Typical experimental profiles of dimensionless channel discharge and cumulative outflow discharge along
627 the side weir (Test N15). The profile of the dimensionless overall discharge in the channel is compared with the ones
628 concerning horizontal strips at different levels (A, B, C, D, E, and F in Fig. 6) above the channel bottom.

629 **Figure 9** – The two velocity-distribution coefficients as a function of the local outflow efficiency: a) energy coefficient
630 α ; b) momentum coefficient β . The solid lines represent polynomial fitting curves of the experimental data.

631 **Figure 10** – Check of the constant energy assumption: ratio of the specific energy at the two ends of the side weir as a
632 function of the Froude number of the incoming flow.

633 **Figure 11** – Comparison of converging side weir flows ($\Theta = -0.12$, $L/b_d = 8.33$) with conventional side weir flows
634 ($\Theta = 0$, $L/B = 8.33$): a) variation of the outflow efficiency η with the Froude number of the onward flow Fr_d for various
635 values of w/h_d ; b) regression analysis of the outflow efficiency on the dimensionless ratio χ ; c) comparison between
636 observed and predicted outflow efficiency.

637 **Figure 12** – Average discharge coefficient \bar{C}_d against Fr_d (a) and Fr_0 (b) for side weir flows in a converging channel
638 ($\Theta = -0.12$, $L/b_d = 8.33$) and in a prismatic channel ($\Theta = 0$, $L/B = 8.33$). c) Cross-plot of $\bar{C}_d / (w/h_d)^2$ versus Fr_0 ; the
639 solid lines represent linear fitting curves of the experimental data.

640 **Figure 13** – Comparison between numerical and experimental water depth and discharge profiles in the main channel
641 for Test N15 [panels a) and b)] and for Test N40 [panels c) and d)].

642 **Figure 14** – Comparison between theoretical, numerical, and experimental free surface profiles in the main channel for
643 a pseudo-uniform flow test case ($\Theta = -0.12$, $\bar{w} = 0.872$, $\bar{C}_d = 0.391$).

644

645

648 Table 1. Test conditions for flow over side weir in a non-prismatic converging channel ($\Theta = -0.12, L/b_d = 8.33$).

Test no.	w (m)	Q_0 (l/s)	h_0 (m)	Fr_0 (-)	Q_d (l/s)	h_d (m)	Fr_d (-)	w/h_d (-)	Q_w (l/s)	\bar{C}_d (-)	η (-)
N1	0.203	19.91	0.231	0.159	8.14	0.233	0.129	0.873	11.77	0.365	0.591
N2	0.203	20.00	0.230	0.160	5.12	0.234	0.080	0.866	14.88	0.447	0.744
N3	0.203	20.01	0.233	0.157	2.97	0.237	0.046	0.855	17.04	0.440	0.852
N4	0.203	19.99	0.235	0.155	1.46	0.239	0.022	0.848	18.53	0.437	0.927
N5	0.203	25.89	0.237	0.199	9.27	0.240	0.140	0.845	16.62	0.377	0.642
N6	0.203	25.78	0.237	0.198	5.56	0.242	0.083	0.839	20.23	0.441	0.784
N7	0.203	25.70	0.240	0.194	3.02	0.245	0.044	0.829	22.68	0.437	0.882
N8	0.203	25.67	0.241	0.192	1.57	0.247	0.023	0.823	24.10	0.437	0.939
N9	0.203	32.82	0.243	0.242	10.53	0.248	0.151	0.819	22.29	0.387	0.679
N10	0.203	32.73	0.243	0.242	6.08	0.250	0.086	0.811	26.65	0.441	0.814
N11	0.203	32.71	0.246	0.238	3.39	0.253	0.047	0.802	29.32	0.439	0.896
N12	0.203	32.73	0.248	0.235	1.70	0.255	0.023	0.797	31.03	0.438	0.948
N13	0.203	42.65	0.249	0.305	11.75	0.255	0.162	0.796	30.90	0.445	0.724
N14	0.203	45.16	0.250	0.320	12.24	0.258	0.166	0.787	32.92	0.442	0.729
N15*	0.183	21.71	0.214	0.195	5.94	0.217	0.104	0.845	15.77	0.410	0.727
N16	0.183	22.07	0.216	0.195	4.55	0.219	0.079	0.835	17.52	0.409	0.794
N17	0.183	21.99	0.219	0.191	2.64	0.222	0.045	0.826	19.35	0.409	0.880
N18	0.183	22.03	0.220	0.190	1.73	0.223	0.029	0.822	20.30	0.413	0.922
N19	0.183	28.12	0.220	0.241	7.13	0.225	0.118	0.812	20.99	0.406	0.746
N20	0.183	27.89	0.221	0.237	4.77	0.226	0.079	0.809	23.12	0.425	0.829
N21	0.183	27.70	0.223	0.233	2.84	0.228	0.046	0.802	24.86	0.424	0.897
N22	0.183	28.11	0.226	0.233	1.86	0.230	0.030	0.795	26.25	0.414	0.934
N23	0.183	33.90	0.225	0.282	8.07	0.232	0.128	0.789	25.83	0.411	0.762
N24	0.183	33.92	0.227	0.279	5.30	0.233	0.083	0.784	28.62	0.430	0.844
N25	0.183	33.94	0.229	0.275	3.06	0.236	0.047	0.777	30.88	0.427	0.910
N26	0.183	33.89	0.230	0.273	1.80	0.237	0.028	0.774	32.09	0.429	0.947
N27	0.183	41.28	0.229	0.335	8.70	0.236	0.134	0.775	32.58	0.460	0.789
N28	0.183	47.81	0.233	0.377	9.81	0.243	0.145	0.753	38.00	0.463	0.795
N29	0.183	58.59	0.240	0.443	11.67	0.254	0.162	0.721	46.92	0.464	0.801
N30	0.153	18.06	0.185	0.201	2.64	0.189	0.057	0.809	15.42	0.373	0.854
N31	0.153	17.98	0.184	0.203	2.03	0.187	0.044	0.817	15.95	0.412	0.887
N32	0.153	17.91	0.185	0.200	1.33	0.188	0.029	0.813	16.58	0.408	0.926
N33	0.153	17.89	0.185	0.199	0.80	0.189	0.017	0.809	17.09	0.404	0.955
N34	0.153	21.96	0.189	0.237	3.17	0.194	0.066	0.789	18.79	0.379	0.856
N35	0.153	21.84	0.186	0.241	2.33	0.192	0.049	0.797	19.51	0.425	0.893
N36	0.153	21.76	0.187	0.239	1.66	0.193	0.035	0.793	20.10	0.424	0.924
N37	0.153	21.73	0.188	0.237	0.86	0.194	0.018	0.790	20.87	0.423	0.960

N38	0.153	34.61	0.200	0.342	4.93	0.209	0.092	0.733	29.68	0.382	0.858
N39	0.153	48.72	0.210	0.449	7.01	0.224	0.117	0.683	41.71	0.399	0.856
N40*	0.153	43.63	0.207	0.411	6.26	0.218	0.109	0.701	37.37	0.388	0.856

649

650

651
652

653 Table 2. Test conditions for flow over side weir in a prismatic channel ($\Theta = 0, L/B = 8.33$).

Test no.	w (m)	Q_0 (l/s)	h_0 (m)	Fr_0 (-)	Q_d (l/s)	h_d (m)	Fr_d (-)	w/h_d (-)	Q_w (l/s)	\bar{C}_d (-)	η (-)
P1	0.203	10.22	0.214	0.183	6.10	0.216	0.108	0.926	4.12	0.336	0.403
P2	0.203	12.01	0.217	0.211	6.41	0.220	0.110	0.921	5.60	0.425	0.466
P3	0.203	14.85	0.220	0.256	7.22	0.224	0.121	0.893	7.63	0.351	0.514
P4	0.203	14.94	0.218	0.260	7.64	0.224	0.127	0.891	7.30	0.351	0.489
P5	0.203	18.12	0.223	0.305	7.91	0.231	0.127	0.880	10.20	0.406	0.563
P6	0.203	19.98	0.227	0.327	8.59	0.235	0.134	0.865	11.39	0.362	0.570
P7	0.183	10.03	0.197	0.204	3.89	0.201	0.077	0.912	6.14	0.457	0.612
P8	0.183	12.75	0.200	0.253	4.47	0.205	0.085	0.891	8.28	0.441	0.650
P9*	0.183	15.04	0.205	0.287	5.23	0.211	0.096	0.869	9.81	0.362	0.653
P10	0.183	17.83	0.204	0.343	5.53	0.213	0.100	0.858	12.30	0.431	0.690
P11	0.183	20.04	0.205	0.382	6.00	0.217	0.106	0.845	14.04	0.426	0.701
P12	0.183	24.83	0.207	0.466	7.01	0.224	0.117	0.818	17.82	0.430	0.718
P13*	0.183	24.67	0.208	0.461	7.45	0.224	0.124	0.816	17.22	0.407	0.698
P14	0.153	8.18	0.171	0.205	1.23	0.173	0.030	0.883	6.95	0.392	0.850
P15	0.153	10.08	0.173	0.248	1.51	0.177	0.036	0.865	8.57	0.388	0.850
P16	0.153	14.86	0.177	0.354	2.33	0.184	0.052	0.834	12.53	0.397	0.844
P17	0.153	14.90	0.177	0.356	2.31	0.184	0.052	0.831	12.59	0.401	0.845
P18*	0.153	16.66	0.176	0.401	2.48	0.186	0.055	0.823	14.18	0.435	0.851
P19	0.153	17.13	0.177	0.409	2.58	0.187	0.057	0.818	14.55	0.424	0.849
P20	0.153	19.66	0.179	0.460	3.14	0.191	0.067	0.802	16.52	0.404	0.840
P21	0.153	19.99	0.179	0.470	3.19	0.192	0.067	0.796	16.80	0.408	0.838
P22	0.153	22.91	0.179	0.535	3.80	0.197	0.077	0.779	19.11	0.407	0.834
P23	0.153	25.21	0.179	0.590	4.35	0.200	0.086	0.765	20.86	0.407	0.828
P24	0.133	15.13	0.159	0.424	0.90	0.169	0.023	0.785	14.23	0.369	0.941
P25	0.133	17.73	0.159	0.497	1.25	0.174	0.031	0.766	16.48	0.377	0.929
P26	0.133	20.27	0.160	0.562	1.63	0.178	0.039	0.749	18.64	0.385	0.919
P27	0.133	22.21	0.159	0.623	1.95	0.181	0.045	0.733	20.26	0.383	0.912
P28	0.133	25.02	0.158	0.704	2.54	0.186	0.056	0.714	22.48	0.385	0.899
P29	0.120	20.67	0.146	0.658	0.86	0.166	0.023	0.723	19.81	0.381	0.958
P30	0.120	22.55	0.144	0.730	1.14	0.172	0.029	0.699	21.41	0.387	0.949
P31	0.120	25.05	0.143	0.825	1.65	0.177	0.039	0.679	23.40	0.386	0.934

654

655

656
657

658 Table 3. Longitudinal variation of significant velocity-distribution variables for Tests N15 and N40.

Section	x (m)	$\frac{1}{A} \frac{\partial A}{\partial x} \Big _{h=\text{const}}$ (m ⁻¹)	Test N15				Test N40			
			α (-)	β (-)	$-\frac{1}{\beta} \frac{d\beta}{dx}$ (m ⁻¹)	φ (°)	α (-)	β (-)	$-\frac{1}{\beta} \frac{d\beta}{dx}$ (m ⁻¹)	φ (°)
I	-1.75	-0.3358	1.019	1.007	-	-	1.017	1.006	-	-
III	-1.35	-0.3522	1.026	1.009	-0.0058	56.7	1.026	1.011	-0.0134	42.9
IV	-1.15	-0.3789	1.032	1.011	-0.0105	56.4	1.032	1.011	+0.0024	42.9
VI	-0.75	-0.4466	1.065	1.023	-0.0284	59.8	1.063	1.021	-0.0256	47.8
VIII	-0.35	-0.5437	1.167	1.058	-0.0831	61.2	1.252	1.088	-0.1528	60.9
IX	-0.15	-0.6101	1.338	1.116	-0.2598	66.2	1.669	1.234	-0.5940	72.9
XI	0.25	-0.6715	1.279	1.094	-	-	1.953	1.288	-	-

659
660
661

662
663

664 Table 4. Global deviation of water depth and discharge numerical profiles from the experimental profiles for Tests N15
665 and N40 assuming that β is either variable along the side weir or uniformly equal to 1.

	Test N15		Test N40	
	$E_h (-)$	$E_Q (-)$	$E_h (-)$	$E_Q (-)$
$\beta = \beta(x)$	$1.79 \cdot 10^{-2}$	$1.610 \cdot 10^{-1}$	$0.694 \cdot 10^{-1}$	$2.813 \cdot 10^{-1}$
$\beta = 1$	$1.19 \cdot 10^{-2}$	$1.758 \cdot 10^{-1}$	$0.802 \cdot 10^{-1}$	$3.014 \cdot 10^{-1}$

666

667

668

669

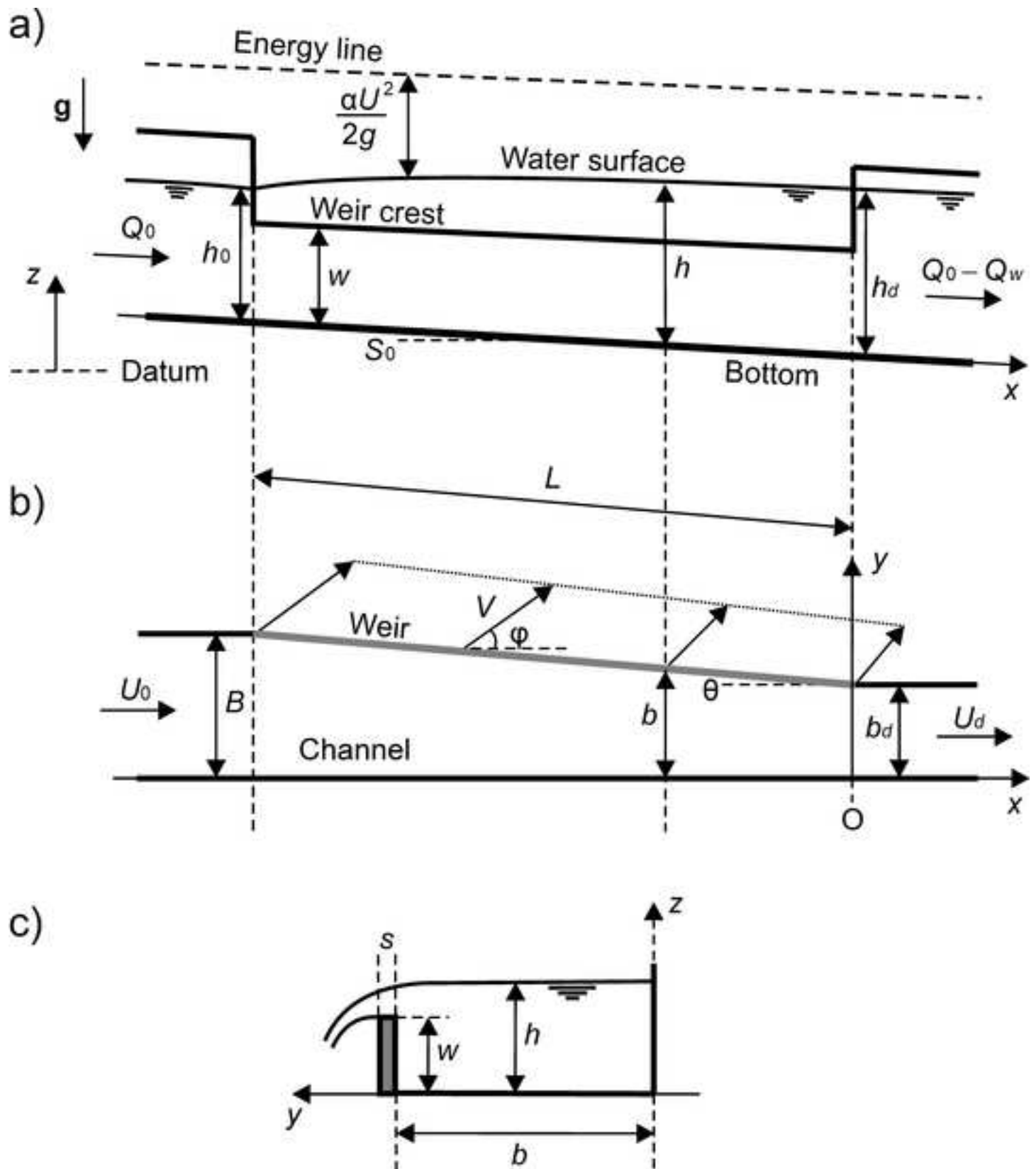
670 **List of table captions**

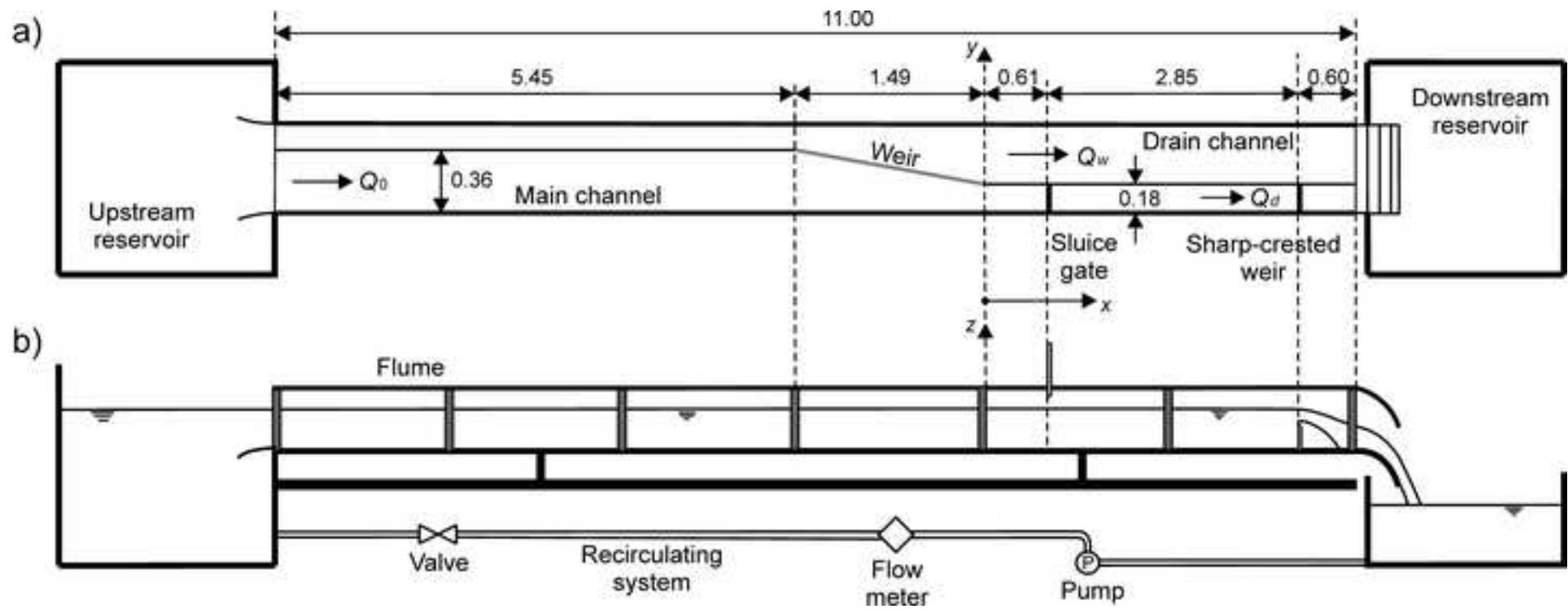
671 **Table 1**– Test conditions for flow over side weir in a non-prismatic converging channel ($\Theta = -0.12$, $L/b_d = 8.33$).

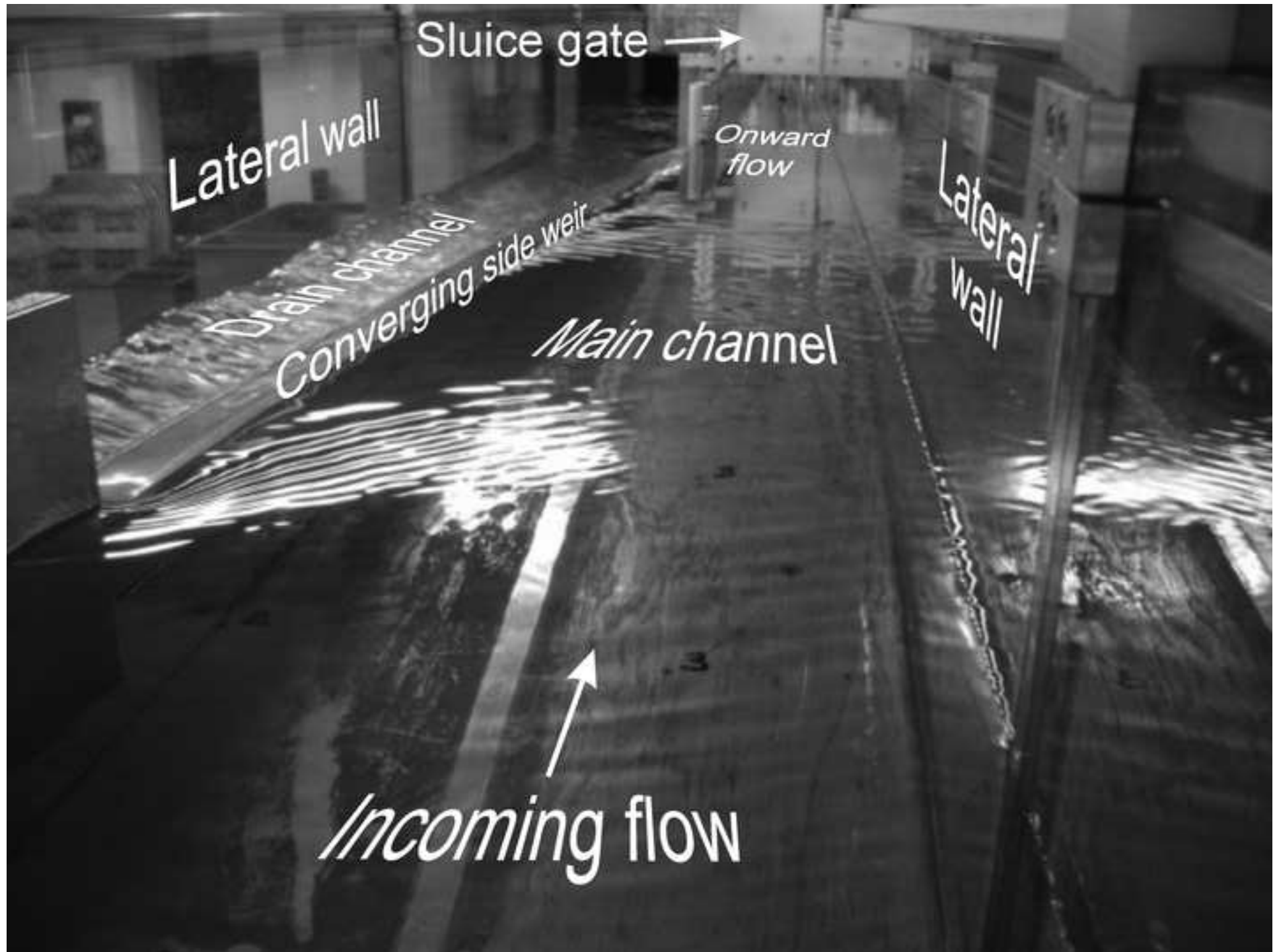
672 **Table 2** – Test conditions for flow over side weir in a prismatic channel ($\Theta = 0$, $L/B = 8.33$).

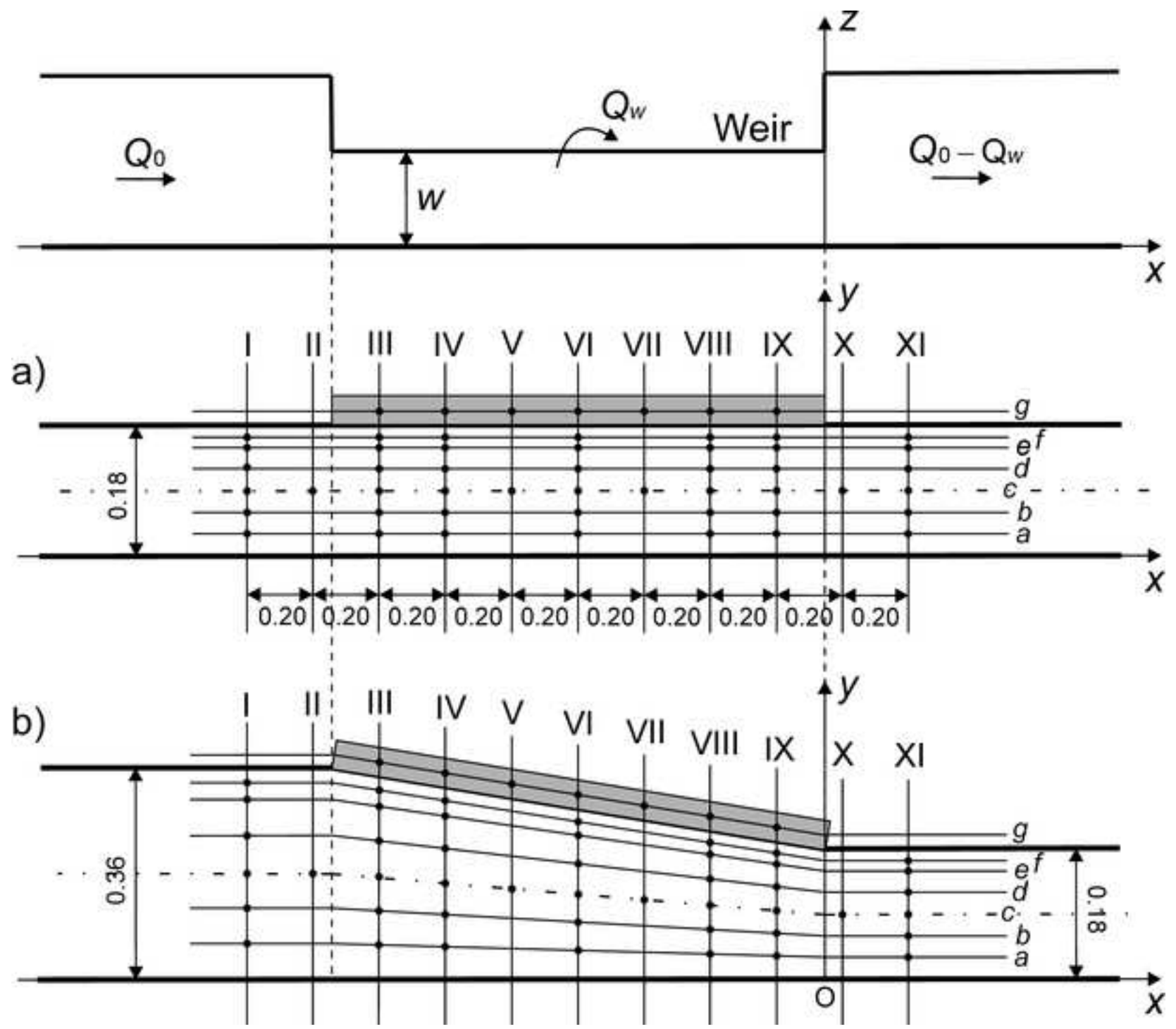
673 **Table 3** – Longitudinal variation of significant velocity-distribution variables for Tests N15 and N40.

674 **Table 4** - Global deviation of water depth and discharge numerical profiles from the experimental profiles for Tests
675 N15 and N40 assuming that β is either variable along the side weir or uniformly equal to 1.









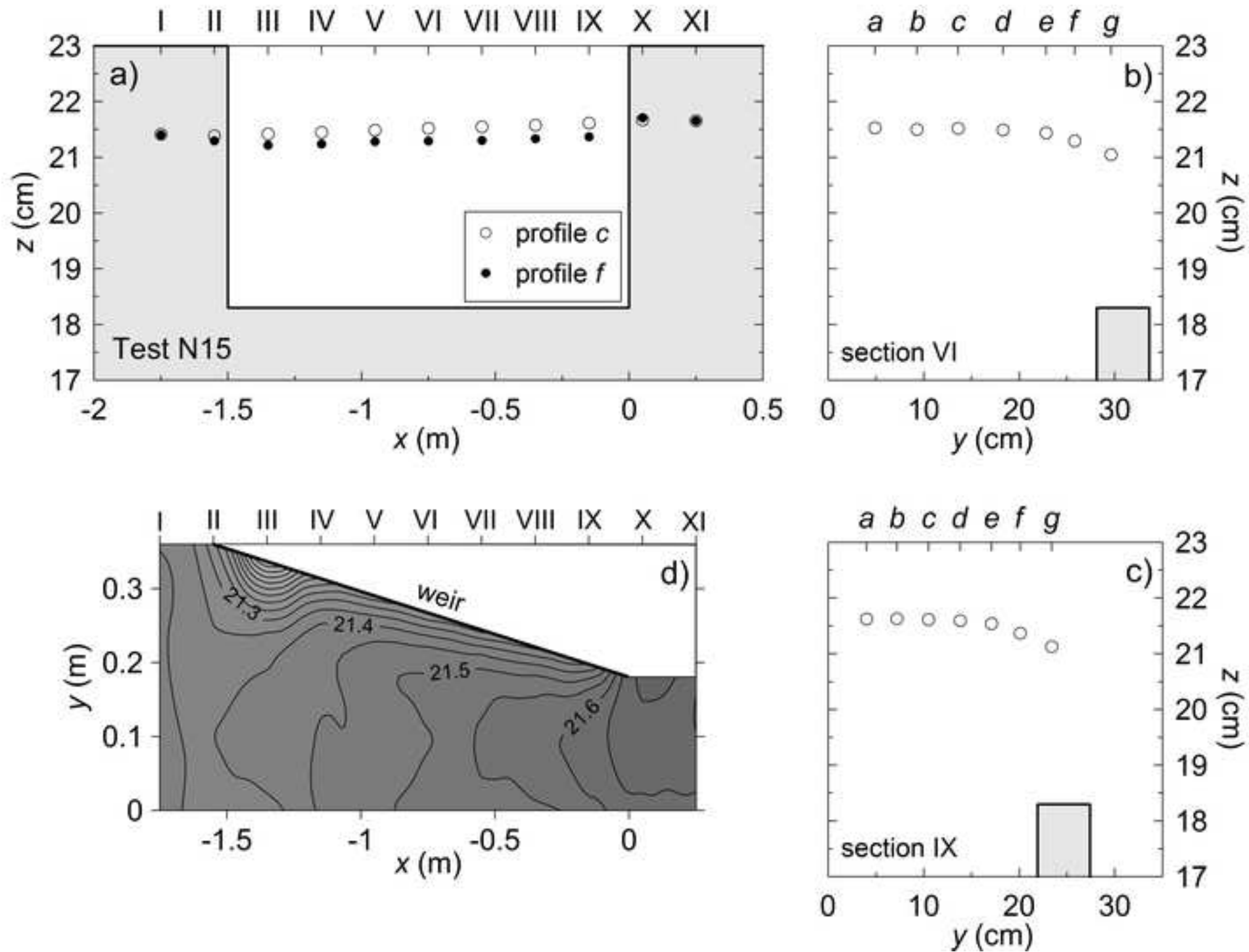


Figure 6

